ETH zürich Universität Zürich[UZH]

Semester Project BSc Physics ETH

The Shadow of a Rotating Black Hole

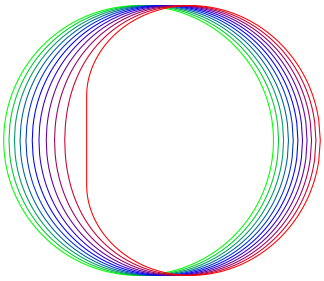

Sébastien C. Garmier
sgarmier@student.ethz.ch

May 22, 2021

Supervisor: Prof. Dr. Philippe Jetzer [1]
Internal ETH member: Prof. Dr. Renato Renner [2]

Abstract The aim of this work is to provide an introduction to the field of shadows of rotating Kerr black holes. We review the mathematics of light propagation in Kerr spacetime and derive the equations describing the edge of a Kerr black hole shadow in the sky of a distant observer. We also discuss recent research concerning the possibility of determining the spin parameter a and the inclination angle θ_O of the observer from direct observations of the shadow. Finally, we showcase two applications of the theory of black hole shadows to the Event Horizon Telescope collaboration image of the supermassive black hole M87*.

[1]Physik-Institut, University of Zürich, Switzerland
[2]Institute of Theoretical Physics, ETH Zürich, Switzerland

Contents

Introduction

A black hole without surrounding matter appears as a perfectly black patch in the sky of an observer, the so-called *black hole shadow*. Synge studied the directions in which light rays can escape from a Schwarzschild black hole as a function of radial distance in 1966 [31], thereby starting the research on black hole shadows. The shadow of a rotating Kerr black hole was then described by Bardeen [4] in 1973, making use of previous work by Carter [7] in 1968 where the propagation of timelike and lightlike geodesics in Kerr spacetime was studied using a Hamilton-Jacobi approach. Luminet later calculated the first realistic image of a Schwarzschild black hole with a thin accretion disk in 1979 [21].

In 2019 the Event Horizon Telescope Collaboration (EHT) published the first real image of a black hole, taken of the supermassive black hole M87* using *very large baseline interferometry* (VLBI) techniques [9] [10] [11]. With the shadow of M87* clearly visible in the image and the prospect of future black hole images, the study of black hole shadows is now more relevant than ever. A natural question to ask is whether the image of a shadow can be used to determine properties of the black hole such as the spin parameter a of a Kerr black hole. Research in the last couple of years [8] [17] [36] has shown that the answer is "yes", given a high enough image resolution. Some estimate that a five-fold increase in resolution from today's EHT resolution would be sufficient [36, section 4].

In this work we aim to provide an introduction to the field of black hole shadows of rotating black holes, focusing on *Kerr black holes*. In section 1 we recall the Kerr metric, describe the Hamilton-Jacobi approach of Carter for the description of null geodesic propagation and introduce the concept of a black hole shadow. In section 2, we derive Bardeen's expressions for the Kerr shadow, cover various special cases and demonstrate the two most

striking features of the shadow: the asymmetric distortion and horizontal displacement of the shadow for rapidly spinning black holes. Section 3 is concerned with methods of determining black hole parameters from the shadow; here we review some of the more recent literature. In section 4 we show the estimate of [36] mentioned above and show how the shadow of M87* has been used to rule out the possibility of M87* being a naked singularity [9].

1 Rotating Black Holes

The Einstein field equations of general relativity allow for *black hole solutions*, also called *black hole metrics*. These spacetimes contain at least one *black hole*, a region from which massive particles and light rays „cannot escape to infinity“. This intuitive definition can be made precise (see for instance [34, chapter 12]). We will however not need this level of sophistication, as we will work with explicit metrics.

We will focus on a particular family of black hole solutions, the so-called *Kerr metric* [19]. Different Kerr black holes are distinguished by two parameters: the mass M and the angular momentum J. If $J \neq 0$, we say the black hole is *rotating*. The Kerr metric describes the exterior of a stationary black hole in an asymptotically flat vacuum spacetime *uniquely*. This follows from a more general theorem: any stationary, asymptotically flat black hole spacetime with a purely electromagnetic stress tensor (an *electrovac* spacetime) is described by a generalization of the Kerr metric, the *Kerr-Newman metric* [23]. Besides M and J, Kerr-Newman black holes are characterized by their electric charge Q, with $Q = 0$ in the Kerr case. This remarkable theorem is called the *no-hair-theorem*. „Hair“ refers to other properties besides M, J and Q such a black hole might have. The no-hair-theorem follows from a long series of results in the 60s and 70s. See [34, section 12.3] for an overview of these results.

Kerr black holes are of interest, if we consider electrically neutral black holes (which is likely to be appropriate, since the universe is electrically neutral at large) and assume that they will eventually settle into a stationary state. We will recall the Kerr solution here.

We note that besides Kerr-Newman, other non-vacuum but still stationary and asymptotically flat black hole solutions exist. See for instance [3] or [2]. And if we drop the requirement of stationarity, many more solutions are of course possible (for instance the highly dynamic spacetime of two merging black holes).

1.1 Kerr Metric

In *Boyer-Lindquist coordinates* (t, r, θ, ϕ), the *Kerr metric* is given by [7]

$$\boldsymbol{g} = \frac{\Sigma}{\Delta}\boldsymbol{dr}^2 + \Sigma \boldsymbol{d\theta}^2 + \frac{\sin^2\theta}{\Sigma}[a\boldsymbol{dt} - (r^2+a^2)\boldsymbol{d\phi}]^2 - \frac{\Delta}{\Sigma}[\boldsymbol{dt} - a\sin^2\theta\ \boldsymbol{d\phi}]^2, \tag{1}$$

where

$$\Delta(r) = r^2 - 2Mr + a^2, \qquad \Sigma(r,\theta) = r^2 + a^2\cos^2\theta.$$

$M \in \mathbb{R}_{\geq 0}$ and $a \in \mathbb{R}$ are the two parameters distinguishing different solutions within the Kerr family. We will mostly use the metric in these coordinates. They are based on coordinates introduced by Boyer and Lindquist [6].

Asymptotic Flatness and Coordinates To understand the meaning of the coordinates, one first notes that the metric is *asymptotically flat*: it is possible to find a coordinate system $(\tilde{t}, \tilde{x}, \tilde{y}, \tilde{z})$ in which the metric becomes $\boldsymbol{g} = -\boldsymbol{d\tilde{t}}^2 + \boldsymbol{d\tilde{x}}^2 + \boldsymbol{d\tilde{y}}^2 + \boldsymbol{d\tilde{z}}^2 + O(1/\tilde{r})$, with $\tilde{r} = [\tilde{x}^2 + \tilde{y}^2 + \tilde{z}^2]^{1/2}$; in fact, the Kerr metric was first given in such coordinates by Kerr in 1963 [19]. In particular, we find $\boldsymbol{g} \to -\boldsymbol{dt}^2 + \boldsymbol{dr}^2 + r^2(\boldsymbol{d\theta}^2 + \sin^2\theta \boldsymbol{d\phi}^2)$, for $r \to \infty$, see [34, section 12.3]. For large r we can therefore view (r, θ, ϕ) as spherical coordinates and

t becomes the time of an observer at infinity. Upon further inspection, (r, θ, ϕ) are more appropriately viewed as *oblate spherical coordinates*, which become spherical at large r.

One accordingly introduces the Cartesian coordinates

$$x = \sqrt{r^2 + a^2} \sin\theta \cos\phi, \qquad y = \sqrt{r^2 + a^2} \sin\theta \sin\phi, \qquad z = r\cos\theta, \tag{2}$$

which are particularly useful for plotting and visualisation purposes.

Mass and Angular Momentum The mass M and angular momentum J of an isolated gravitating system is *a priori* defined only in the weak field limit and can be calculated using suitable integrals of the energy-momentum tensor $\boldsymbol{T}$. It is also possible to extract M and J from an expansion of the metric in powers of (distance to centre of mass)$^{-1}$. In practice, this allows one to measure M and J from the effect of the metric on test particles and gyroscopes at large distances from the system. Such an expansion is also possible in asymptotic flat spacetimes, even for strong fields. One can extend the meaning of mass and angular momentum in this way. In particular, asymptotically flat *vacuum* spacetimes ($\boldsymbol{T} = 0$) can be assigned a mass M and an angular momentum J. See [22, chapter 19].

One finds that the central mass of the Kerr metric is the parameter M (hence the choice of symbol) and the angular momentum is $J = Ma$. This is what is meant by the „mass and angular momentum of the black hole“. See [22, section 33.3]

Schwarzschild Case If we set $a = 0$, we obtain the *Schwarzschild metric*:

$$\boldsymbol{g} = -\left(1 - \frac{2M}{r}\right)\boldsymbol{dt}^2 + \left(1 - \frac{2M}{r}\right)^{-1}\boldsymbol{dr}^2 + r^2\boldsymbol{d\theta}^2 + r^2\sin^2\theta\ \boldsymbol{d\phi}^2. \tag{3}$$

This family of black hole solutions was the first to be found, in 1916 by Schwarzschild [28].

Event Horizons The condition $\Delta = 0$ yields singularities at

$$r_\pm = M \pm \sqrt{M^2 - a^2}. \tag{4}$$

These are mere coordinate singularities and become the familiar Schwarzschild coordinate singularity $r = 2M$ in the $a = 0$ case. The condition $\Sigma = 0$ on the other hand yields a real singularity (it will not concern us however). The hypersurfaces $r = r_\pm$ are *event horizons* that can only be traversed in the direction of decreasing r by timelike or null curves. This is why the Kerr metric is a black hole solution. In the so-called *extremal case* $a = M$, both horizons coincide. For $a > M$, no horizon exists; the singularity $\Sigma = 0$ is then called *naked*. See for instance [34, section 12.3]. We will only consider $r \geq r_+$. The „inner horizon“ at r_- will be unimportant for us.

Killing Vector Fields We recall that a vector field $\boldsymbol{\xi}$ is a *Killing vector field* of the metric $\boldsymbol{g}$, if the flow it generates preserves the metric: i.e. $\mathcal{L}_{\boldsymbol{\xi}}\boldsymbol{g} = 0$. Killing vector fields and their associated isometry groups thus encode the one-parameter symmetries of a given spacetime. The condition $\mathcal{L}_{\boldsymbol{\xi}}\boldsymbol{g} = 0$ amounts to *Killing's equation*: $\boldsymbol{g}(\nabla_{\boldsymbol{Y}}\boldsymbol{\xi}, \boldsymbol{Z}) + \boldsymbol{g}(\boldsymbol{Y}, \nabla_{\boldsymbol{Z}}\boldsymbol{\xi}) = 0$ for all vectors $\boldsymbol{Y}$ and $\boldsymbol{Z}$. A coordinate vector field $\boldsymbol{\partial_\alpha}$ being a Killing vector field is equivalent to $\partial_\alpha g_{\mu\nu} = 0$. Since the Kerr metric does not depend on the coordinates t and ϕ, both $\boldsymbol{\partial_t}$ and $\boldsymbol{\partial_\phi}$ are Killing vector fields. See for instance [34, appendix C & section 12.3].

Stationarity and Ergosphere An asymptotically flat metric is called *stationary*, if it has a Killing vector field $\boldsymbol{\xi}$ which is timelike [34, section 6.1].

$\boldsymbol{\partial_t}$ is timelike for $r > r_E(\theta)$, where

$$r_E(\theta) = M + \sqrt{M^2 - a^2\cos^2\theta} \tag{5}$$

is the *static limit*. The region $r_+ < r < r_E$ is called the *ergosphere*. The Kerr metric is thus stationary outside r_E. At $r = r_E$, $\boldsymbol{\partial_t}$ is lightlike, and for $r_+ \leq r < r_E$ it is spacelike. Observers at rest relative to the coordinates (r, θ, ϕ) can only exist for $r > r_E$, because otherwise their necessarily timelike four-velocity would be a multiple of the non-timelike $\boldsymbol{\partial_t}$. Within the ergosphere, any timelike curve must inevitably follow $d\phi/d\tau > 0$ (if $a > 0$; if $a < 0$, the inequality is reversed). See [34, section 12.3].

The ergosphere provides an extreme case of the *Lense-Thirring effect*, whereby timelike and null geodesics with zero angular momentum L (see next section) in a Kerr spacetime with $a \neq 0$ do not correspond to $\phi = \text{const}$. [34, p. 187]. This effect also leads to a precession of gyroscopes, which is one of the ways one can measure a in practice [22, section 33.3].

Axial Symmetry The Killing vector field $\boldsymbol{\partial_\phi}$ gives rise to closed, spacelike integral curves; they are rings with $t, r, \theta = \text{const}$. We thus say that the Kerr metric is *axially symmetric* [34, section 7.1]. This terminology also makes sense in light of the interpretation of (θ, ϕ) as coordinates on the unit sphere, since $\boldsymbol{g}$ does not depend on the azimuth ϕ.

Spherical Symmetry of the Schwarzschild Metric The Schwarzschild case $a = 0$ is not just axially symmetric, but *spherically* symmetric. We can reorient the plane $\theta = \pi/2$ arbitrarily by coordinate rotations and we will always find the killing vector field $\boldsymbol{\partial_\phi}$ [3].

1.2 Null Geodesics in Kerr Spacetime

Light rays are null geodesics, following the geodesic equation $\nabla_{\boldsymbol{u}} \boldsymbol{u} = 0$. We review the most important features of null geodesics in Kerr spacetime here. Knowledge of null geodesic motion is the basis for our discussion of black hole shadows.

Constants of Motion from Killing Vector Fields If $\boldsymbol{\xi}$ is a Killing vector field and $\boldsymbol{u}$ is the tangent to a geodesic (recall that geodesics are affinely parametrised), one finds that the quantity $\boldsymbol{g}(\boldsymbol{\xi}, \boldsymbol{u})$ is constant along the geodesic. This follows from Killing's equation and the geodesic equation $\nabla_{\boldsymbol{u}} \boldsymbol{u} = 0$.

We thus find two constants of motion in Kerr spacetime:

$$E = -\boldsymbol{g}(\boldsymbol{u}, \boldsymbol{\partial_t}) = \left(1 - \frac{2Mr}{\Sigma}\right) u^t + \frac{2Mar \ \sin^2\theta}{\Sigma} u^\phi, \tag{6}$$

$$L = \boldsymbol{g}(\boldsymbol{u}, \boldsymbol{\partial_\phi}) = -\frac{2Mar \ \sin^2\theta}{\Sigma} u^t + \frac{(r^2 + a^2)^2 - \Delta a^2 \ \sin^2\theta}{\Sigma} \sin^2\theta \ u^\phi. \tag{7}$$

We refer to E as the *energy* and to L as the *angular momentum* of the geodesic [4]. Given E and L, typically from initial conditions, we can solve (6) and (7) for u^t and u^ϕ. The second order geodesic equations for t and ϕ are thus replaced with two simpler first order equations. See [34, section 12.3].

Third Constant As a consequence of the geodesic equation and the Levi-Civita property $\nabla \boldsymbol{g} = 0$ of the covariant derivative, we find that $\boldsymbol{g}(\boldsymbol{u}, \boldsymbol{u})$ is another conserved quantity. For null geodesics we have

$$\boldsymbol{g}(\boldsymbol{u}, \boldsymbol{u}) = 0. \tag{8}$$

[3] More precisely, the Schwarzschild metric posses an isometry group isomorphic to $SO(3)$. Because this is not a one-parameter group, the symmetry cannot be described solely by a Killing vector field. It requires three generators.

[4] If we choose $\boldsymbol{u}$ to be the wave vector, then $\hbar E$ and $\hbar L$ are the energy and angular momentum, with respect to the black hole, that an observer at infinity would measure per photon (assuming the geodesic extends to infinity). This justifies the names given to E and L. A similar correspondence holds between E and L of timelike geodesics and specific particle energy and angular momentum at infinity.

Carter's Constant To rewrite all four geodesic equations as first order equations, we need another conserved quantity besides (6), (7) and (8). Such a constant was found in 1968 by Carter [7] (using the metric in a coordinate system other than Boyer-Lindquist, however). Since much of what follows will be based on this result, we give Carter's argument, but adapt it to Boyer-Lindquist coordinates [5].

The geodesic equations can be derived from the Lagrangian $L = \frac{1}{2}\boldsymbol{g}(\boldsymbol{u}, \boldsymbol{u})$. The conjugate momentum one-form is $\boldsymbol{p} = \boldsymbol{g}(\boldsymbol{u}, \cdot)$ and the Hamiltonian therefore

$$H(\boldsymbol{p}) = \boldsymbol{p}[\boldsymbol{u}] - L = \frac{1}{2}\boldsymbol{g}(\boldsymbol{u}, \boldsymbol{u}) = \frac{1}{2}\boldsymbol{g^{-1}}(\boldsymbol{p}, \boldsymbol{p}), \tag{9}$$

where $\boldsymbol{g^{-1}}$ is the inverse metric tensor. Being a multiple of (8), H is constant along geodesics. It is identically zero for null geodesics (although we still keep the H's in our calculations for now). In our notation we have omitted that $H(\boldsymbol{p}) = H(x^\mu, \boldsymbol{p})$ is more accurately also a function of position.

With the geodesic parameter denoted by λ, Hamilton's equations read $dp_\mu/d\lambda = -\partial H/\partial x^\mu$ and $dx^\mu/d\lambda = \partial H/\partial p_\mu$. They yield second order equations for r and θ as well as two constants of motion $p_t = \text{const.}$ and $p_\phi = \text{const.}$, since the metric and thus the Hamiltonian do not depend on t and ϕ. These constants are however nothing but the already known constants of motion: $p_t = -E$ and $p_\phi = L$.

To find a fourth motion constant, we take a Hamilton-Jacobi approach. We recall (see for instance [20]) that a sufficiently general solution $S(\lambda, x^\mu)$ to the *Hamilton-Jacobi equation*

$$\frac{\partial S}{\partial \lambda} + H\left(\boldsymbol{d}S\right) = 0 \tag{10}$$

determines the momentum of trajectories via $\boldsymbol{p} = \boldsymbol{d}S$. If the Hamilton-Jacobi equation can be separated, the separation constant immediately gives a motion constant.

In order to compute $H(\boldsymbol{d}S)$, we need the covariant components $g^{\mu\nu}$ of the metric; they can be readily found using the Boyer-Lindquist form (1) of the metric. The Hamilton-Jacobi equation then becomes

$$\begin{aligned} -\Sigma\frac{\partial S}{\partial \lambda} = &-\frac{1}{2\Delta}\left[(r^2+a^2)\frac{\partial S}{\partial t} + a\frac{\partial S}{\partial \phi}\right]^2 + \frac{\Delta}{2}\left(\frac{\partial S}{\partial r}\right)^2 \\ &+ \frac{1}{2\sin^2\theta}\left[\frac{\partial S}{\partial \phi} + a\sin^2\theta\frac{\partial S}{\partial t}\right]^2 + \frac{1}{2}\left(\frac{\partial S}{\partial \theta}\right)^2. \end{aligned} \tag{11}$$

Taking into account that $\partial S/\partial t = p_t = -E$, $\partial S/\partial \phi = p_\phi = L$ and $\partial S/\partial \lambda = -H$ are constants of motion, and recalling the definitions (1) of Δ and Σ, we find that the equation can be separated in r and θ. This yields the separation constant

$$\mathscr{K} = p_\theta^2 - 2Ha^2\cos^2\theta + \frac{1}{\sin^2\theta}[L - aE\sin^2\theta]^2 = -\Delta p_r^2 - 2Hr^2 + \frac{1}{\Delta}[La - E(r^2+a^2)]^2, \tag{12}$$

a new constant of motion. Carter also introduced a slight variation thereof:

$$\mathscr{Q} = \mathscr{K} - (L - aE)^2 = p_\theta^2 + \cos^2\theta\ [a^2(-2H - E^2) + L^2/\sin^2\theta]. \tag{13}$$

$\mathscr{Q}$ is called the *Carter constant*.

We can now express p_θ^2 in terms of θ only. Equivalently, $p_\theta = \Sigma u^\theta$ is determined *up to sign*:

$$\Sigma u^\theta = \pm\sqrt{\Theta}, \qquad \Theta = \mathscr{Q} - \cos^2\theta\ [a^2(-2H - E^2) + L^2/\sin^2\theta]. \tag{14}$$

Similarly, we find that (with $p_r = \Sigma\Delta^{-1}u^r$):

$$\Sigma u^r = \pm\sqrt{R}, \qquad R = [E(r^2+a^2) - La]^2 - \Delta[(L - aE)^2 - 2Hr^2 + \mathscr{Q}]. \tag{15}$$

[5] [22, Exercise 33.7] essentially covers this adaptation.

Form of S As an aside we note that S must be of the form

$$S = -H\lambda - Et + L\phi + S_r(r) + S_\theta(\theta), \tag{16}$$

where $S_r(r)$ and $S_\theta(\theta)$ are yet to be determined. The term $-H\lambda$ follows from the Hamilton-Jacobi equation and $H = \text{const}$. The term $-Et$ follows from $\partial S/\partial t = (\boldsymbol{d}S)_t = p_t = -E = \text{const}$. The term $+L\phi$ comes similarly. The form of the last two terms follows from the separation of r and θ. Using $p_\theta = \partial S/\partial\theta$, we find that $S_\theta(\theta) = \pm\int\sqrt{\Theta}\,d\theta$. Similarly, $S_r(r) = \pm\int\Delta^{-1}\sqrt{R}\,dr$.

Special Properties of Null Geodesics For null geodesics, we have $H = 0$. This leads to a range of additional properties specific to null geodesics, which will be useful later.

Dividing equations (15) and (14) by E, interpreting the changes $u_r \rightsquigarrow u_r/E$ and $u_\theta \rightsquigarrow u_\theta/E$ as a re-parametrization of the geodesic and setting $H = 0$, we find that the right hand sides no longer depend on all three constants E, L and $\mathscr{Q}$, but only on the ratios

$$\xi := \frac{L}{E}, \qquad \eta := \frac{\mathscr{Q}}{E^2}. \tag{17}$$

For null geodesics, only ξ and η are independent of each other. We shall therefore use the ratios instead of E, L and $\mathscr{Q}$. See [4, section III].

With $H = 0$ it follows from (12) that $\mathscr{K} \geq 0$ and from (13) that $\eta \geq -(\xi - a)^2$. All null geodesics that reach the equator at $\theta = \pi/2$ require $\eta \geq 0$, because Θ cannot be negative in equation (14). Furthermore, any geodesic passing the equator ($p_\theta \neq 0$ at $\theta = \pi/2$) must fulfil $\eta > 0$. Some null geodesics that never reach the equator can have $\eta < 0$. They require $-a^2 + \xi^2/\sin^2\theta < 0$ for all values of θ reached; a simpler necessary condition we will use is $\xi^2 < a^2$. See [7].

Full Set of first Order Equations The equations (6) and (7) provide first order equations for t and ϕ along null geodesics. Similarly, (14) and (15) provide first order equations for θ and r; although the latter two cannot fully predict geodesic motion at $u_r = 0$ or $u_\theta = 0$, where the second order geodesic equations are needed. The constants ξ and η (or alternatively, E, L and $\mathscr{Q}$) can be determined from initial conditions.

1.3 Qualitative Features of Light Deflection, Shadows

A well-known consequence of general relativity is the deflection of light rays by gravity, first described by Einstein [14] for weak gravitational fields. This phenomenon is also called *gravitational lensing*. Light deflection also happens in Kerr spacetime. We can solve the geodesic equations numerically for different initial conditions and plot the resulting rays for quick visual insight into how light is deflected in Kerr spacetime; for example, figure 1 shows numerically computed light rays in the equatorial plane of a Kerr black hole with $M = 1$ and $a = 0.8$. In the figure, the black hole is spinning counterclockwise. One can clearly see the bending of rays and also the influence of the Lense-Thirring effect.

Shadow of the Black Hole If we let the light rays "run in reverse", that is $u^r \rightsquigarrow -u^r$, $u^\theta \rightsquigarrow -u^\theta$, $u^\phi \rightsquigarrow -u^\phi$, but $u^t \rightsquigarrow u^t$, we get new curves. In flat spacetime, such reversed light rays are also null geodesics, since any path taken by light in one direction is also possible in the opposite direction. This is however not true in Kerr spacetime: from equations (6), (7), (13), (14) and (15) we find that we must also replace a with $-a$ in order for the reversed light rays to be null geodesics (also, we then have $\xi \rightsquigarrow -\xi$ and $\eta \rightsquigarrow \eta$). Intuitively, the same effect can be achieved by "reversing time" ($t \rightsquigarrow -t$), but then the "rotation" of the black hole must also be reversed.

The light rays of figure 1 can thus also be interpreted as leaving towards the left, with the black hole spinning clockwise. Such a parallel bundle of rays leaving to infinity is a good

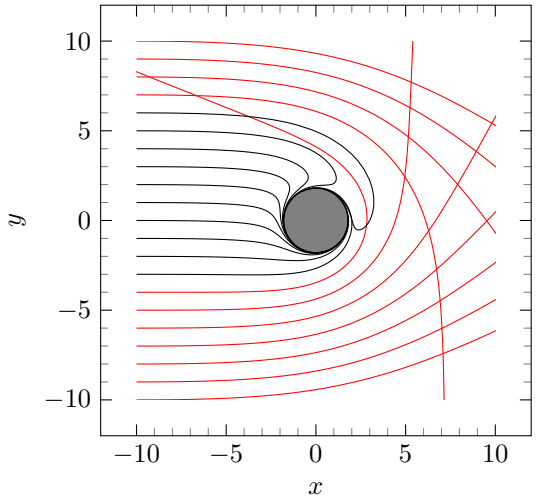

Figure 1: Equatorial plane of a Kerr black hole ($M = 1$, $a = 0.8$, counterclockwise rotation, Cartesian coordinates are used). The region within the outer event horizon is shaded. Incoming light rays from the left are deflected and either escape to infinity (red rays) or fall into the black hole (black rays). The rays were computed using the `cuRRay 2` raytracing code (available at `https://gitlab.com/sebiG/curray2-dev`). The software numerically integrates the geodesic equation from initial conditions using the adaptive *Dormand-Prince* fourth/fifth-order method [12].

approximation of what an observer sufficiently far away sees in their sky when looking at the black hole. Let us assume an empty universe except for the black hole, the observer and a radiation background. The red rays then correspond to light rays arriving at the observer from the radiation background, while the black rays originating at the event horizon are infinitely redshifted and will form a black region in the observer's sky.

This black patch amid the otherwise visible background radiation in the sky of the observer is called the *shadow of the black hole*, as seen by that observer. From the figure we can see that the shadow of a Kerr black hole will generally not be symmetrical with respect to the centre of the black hole. Since the shadow is completely black, it is completely described by the *limit curve* between shadow and background in the observer's sky, the *shadow edge*. The edge consists of light rays that when traced backwards circle indefinitely around the black hole, never falling in but also never escaping (see [4, section III]). Most of what follows will be concerned with the shadow edge.

Lensing Ring The infinitely circling light rays making up the shadow edge imply the existence of light rays nearby that circle many times before reaching the observer. In a region of sky near the shadow we thus see rays circling n times, $n + 1$ times, etc., up to arbitrarily high numbers of orbits. Since the images of these rays approach the shadow edge, they must be spaced very narrowly and lie close to the shadow for high n. See [21] (Schwarzschild case, which however generalizes to Kerr). They are thus perceived as a single, bright ring of extremely lensed light. In some observational situations it might be easier to detect this lensing ring rather than the shadow edge [36, section 5]. We however lose no generality when only considering the shadow edge, since the lensing ring effectively coincides with it.

2 Computation of Shadows

Given any observer O in some Kerr spacetime, we can ask for the shape of the black hole shadow this observer would see. Clearly we need to know the parameters (M, a) of the spacetime for this, but also the coordinates (r_O, θ_O) of the observer and their four-velocity $\boldsymbol{u_O}$ (to keep track of aberration). The metric does not depend on t or ϕ, so neither does the motion of geodesics. We therefore do not need t_O and ϕ_O to compute the shadow.

The shadow of a Kerr black hole was first given in an analytical form by Bardeen [4] in 1972. More recently, this method was adapted to fit more general, not necessarily vacuum, rotating spacetimes (for instance [33], [29] and references therein). If analytical results are not required, the shadow can also be numerically computed using raytracing [8].

We will focus on the shadows of Kerr black holes. In section 2.1, we follow Bardeen's original argument to derive the analytical expressions of the shadow edge. We use them to compute shadows of Kerr black holes in section 2.2 and describe the two most striking features of the shadows semi-analytically: the displacement of the shadow from the symmetry axis of the gravitational field and the asymmetry of the shadow.

2.1 Analytical Expression for the Shadow of a Kerr Black Hole

We will loosely follow the original argument presented in [4, section III] and flesh out some details. Major departures from the original argument are marked as such. Following Bardeen, we consider a Kerr black hole with $a \leq M$ and an observer O at a very large radial coordinate r_O (in the asymptotic region of spacetime), but at arbitrary polar coordinate θ_O. We also assume O to be at rest relative to the Boyer-Lindquist coordinates [6]; this is possible, since O is well outside the ergosphere.

Sky of the Observer The field of view of O consist of light rays incoming from different directions in the sky of O. We label these directions by the angular displacement $\tilde{\alpha}$ perpendicular from the axis of symmetry of the spacetime and the angular displacement $\tilde{\beta}$ from the centre of the spacetime along the axis of symmetry. The location in the sky of the symmetry axis and the centre is determined by the asymptotic behaviour of the gravitational field at O. We choose the direction of $\tilde{\alpha}$ such that the side of the black hole nearest to O "rotates" from negative $\tilde{\alpha}$ to positive, and the direction of $\tilde{\beta}$ such that positive $\tilde{\alpha}$, positive $\tilde{\beta}$ and the direction from the spacetime centre to the observer form a right-handed system.

Since r_O is large, the shadow of the black hole will be small in angular size: $\tilde{\alpha}$ and $\tilde{\beta}$ are roughly inversely proportional to r_O. It therefore makes sense to define the impact parameters $\alpha := r_O\tilde{\alpha}$ and $\beta = r_O\tilde{\beta}$. We find for an incoming light ray with motion constants ξ and η (see appendix A for details):

$$\alpha = -\xi / \sin\theta_O, \tag{18}$$

$$\beta = \pm\sqrt{\eta + a^2\cos^2\theta_O - \xi^2\cot^2\theta_O}. \tag{19}$$

In [4, section III], the square root and a^2 in β are missing in what is most likely a print mistake (they are again in place later on and the more general analysis of [33] also leads to (18) and (19) in the case of a Kerr black hole).

The position (α, β) in the observer's sky of an incoming light ray is thus almost uniquely determined by the constants of motion of the ray. Only a sign uncertainty remains for β, stemming from the sign uncertainty in (14); hence, two incoming light rays exist for each possible set of motion constants, one with positive β, one with negative β (or just one, if $\beta = 0$).

We note that the expressions for α and β break down at $\theta_O = 0$ and $\theta_O = \pi$. These cases will be dealt with specifically later on.

[6] This sets $\boldsymbol{u_O}$. But we can always switch to a different value using a Lorentz boost, if required.

Conditions for Photon Orbits As remarked in section 1.3, the edge of the shadow consist of light rays that when traced backwards, circle the black hole indefinitely. We call these geodesics *photon orbits*. Knowing which values of ξ and η correspond to photon orbits will then provide us the coordinates (α, β) of points in the shadow's edge via equations (18) and (19). The light rays in photon orbits actually never reach the observer; rather, their absence in the sky is noticed as the outermost part of the shadow.

A photon orbit must be bounded in the r coordinate from above and below. It can be shown from equation (15), that the radial motion of any null geodesic outside the horizon has *at most one turning point* (see appendix A). Any null geodesic with a radial turning point thus cannot be a photon orbit, as it will either fall into the black hole ($u^r < 0$ after turning point) or escape to infinity ($u^r > 0$ after turning point). A null geodesic is therefore a photon orbit if and only if $u^r = 0$ everywhere along the orbit.

Equivalently (see appendix A), a null geodesic is an orbit if and only if the conditions

$$R = 0 \tag{20}$$

and

$$\frac{\partial R}{\partial r} = 0 \tag{21}$$

hold *for at least one point* on the geodesic.

It is of course impractical to check every possible null geodesic against these conditions. We rather seek values of r which simultaneously satisfy (20) and (21) for common values of η and ξ. These will include all radii of photon orbits as well as some "imposter" solutions which would require impossible values or combinations of ξ and η. The physical solutions (triplets r, ξ, η) can then be used to produce the shadow outline.

It is interesting to mention that Kerr photon orbits are more intricate than Schwarzschild photon orbits; for instance, they are not confined to a plane and (as we shall see) can exist at a range of radial coordinates. See [32] for a treatment and various illustrations of Kerr photon orbits.

Photon Orbit Candidates Combining the conditions, we get η in terms of ξ and r:

$$\eta = r^2 \frac{3r^2 + a^2 - \xi^2}{r^2 - a^2}, \tag{22}$$

as well as a quadratic equation for ξ yielding

$$\xi_\pm = \frac{M(r^2 - a^2) \pm r\Delta}{a(r - M)} \tag{23}$$

(see appendix A for details). The equations (22) and (23) give use the motion constants $\xi_\pm(r)$ and $\eta_\pm(r)$ of a potential photon orbit at radius r. As already mentioned, not all combinations of ξ and η are allowed and hence not all values of r allow for photon orbits.

The solution $\xi_+ = (r^2 + a^2)/a > a$ leads to $\eta_+ = -r^4/a^2$. This implies $\mathscr{K}/E^2 = \eta_+ + (\xi_+ - a)^2 = 0$, which due to (12) in turn requires $\xi_+ = a\sin^2\theta \leq a$, a contradiction (argument based on [33]). Only

$$\xi_- = \frac{M(r^2 - a^2) - r\Delta}{a(r - M)} \tag{24}$$

and the corresponding

$$\eta_- = \frac{r^3}{a^2(r - M)^2}[4a^2M - r(r - 3M)^2] \tag{25}$$

can yield physical results. From now on, we will refer to ξ_- and η_- simply as ξ and η.

Range of r and Equatorial Orbits We now seek the range of allowed radii r. We have already seen that $\eta > -(\xi - a)^2$ for photon orbits. For $\eta \geq 0$, no further restrictions apply. As for the possibility $\eta < 0$, we intuitively expect all photon orbits to cross the equator [7], which would forbid $\eta < 0$. Appendix A shows that our suspicions are indeed true; roughly speaking, the condition $\xi^2 < a^2$ for the case $\eta < 0$ turns out too restrictive. Thus: all photon orbits cross the equator or remain at the equator, and $\eta \geq 0$ always.

Since we are only interested in orbits outside the horizon, a final requirement is $r \geq r_+$. The allowed values of r are then precisely the values of r outside the horizon at which $\eta(r)$ in (25) is greater or equal to zero. Orbits with $\eta(r) = 0$ must lie entirely at the equator and we call them *equatorial orbits* (this agrees with $\partial\Theta/\partial\theta = 0$ at the equator).

Starting from here, our approach slightly differs from Bardeen's. The sign of $\eta(r)$ is determined by $f(r) = 4a^2M - r(r-3M)^2$, since the prefactor is always positive for $r > r_+$. f is a third degree polynomial with three real roots:

$$r_{\mathrm{ph}\pm} = 2M\left[1 + \cos\left(\frac{2}{3}\arccos(\mp a/M)\right)\right] \geq r_+ \tag{26}$$

and

$$r_3 = 2M\left[1 + \cos\left(\frac{2}{3}\arccos(a/M) + 2\pi/3\right)\right] \leq r_+. \tag{27}$$

These expressions *a prior* only work for $a < M$: $r_{\mathrm{ph}+} = r_+$ is not a zero of η if $a = M$. We will come back to this later. Figure 2 shows the roots.

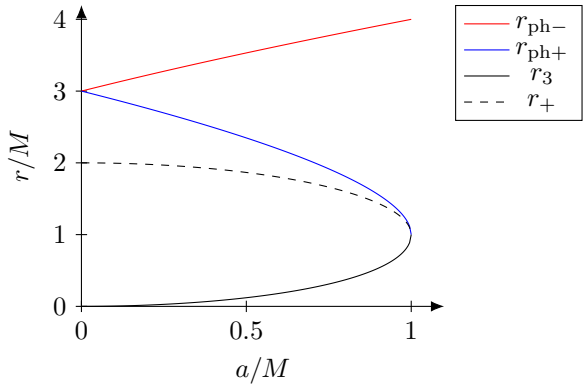

Figure 2: $r_{\mathrm{ph}+}$, $r_{\mathrm{ph}-}$ and r_3 as functions of a/M compared to the event horizon radius r_+.

It is clear that since $r_3 < r_+$ for all values of $a/M < 1$, it must be discarded $r_{\mathrm{ph}+}$ corresponds to an equatorial photon orbit with $\xi > 0$. We call it the *prograde* equatorial orbit, as it runs in the same direction as the black hole spin. Similarly, $r_{\mathrm{ph}-}$ corresponds to a *retrograde* equatorial orbit, with $\xi < 0$. We note that $r_{\mathrm{ph}+} < r_{\mathrm{ph}-}$ if $a \neq 0$. This can intuitively be understood using the Lense-Thirring effect: the retrograde orbit „struggles" against the *dragging of inertial frames* in ϕ-direction and runs „slower" in terms of $d\phi/dt$; in order to not fall into the black hole, it must be further away than the prograde orbit. A quick sign check reveals that $f(r) > 0$ only for $r_{\mathrm{ph}+} < r < r_{\mathrm{ph}-}$ and for $r < r_3$. The allowed values of r are thus $r_{\mathrm{ph}+} \leq r \leq r_{\mathrm{ph}-}$.

Bardeen instead obtains the radii of the equatorial photon orbits via a discussion of timelike orbits in the equatorial plane in the limit where the particle mass becomes zero. This is akin to the procedure one often uses (see for instance [22, chapter 25] and [34, section 6.3]) for the discussion of general orbits in Schwarzschild spacetime. Bardeen then arrives at the same range of allowed radii as we do, see [4, section II]. Since we are not interested in timelike orbits, we chose a more direct approach.

[7] Otherwise, there would have to be some unexpected repulsive effect in the θ direction at the equator.

Computation of the Shadow Outline By inserting the allowed values for r into the equations (24) and (25), we find the values of ξ and η corresponding to photon orbits. Equations (18) and (19) then tell us where in the sky of the observer rays with these ξ and η appear. As discussed before, the locus of these positions is exactly the edge of the shadow. This locus is symmetrical with respect to the α axis, because two values of β are possible for each distinct pair (ξ, η). The area enclosed by the edge appears black and the area outside is filled with background radiation.

The case $\theta_O = \pi/2$ and $a = M$ was explicitly demonstrated in [4, section III]. For more general cases, we also have to consider that not all values of ξ and η might lead to rays incoming at O, even if ξ and η are otherwise allowed; for instance, equatorial rays can never reach observers with $\theta_O \neq \pi/2$. A ray with given (ξ, η) exists at O, if the corresponding α and β are real numbers; we must thus ignore pairs (ξ, η) where the expression in the square root of (19) is negative. By solving

$$\eta(r) + a^2 \cos^2 \theta_O - \xi(r)^2 \cot^2 \theta_O = 0 \tag{28}$$

for r, we get the minimum and maximum photon orbit radii, which are relevant for the chosen observer position θ_O. This requires solving a fifth-order polynomial and is thus best done numerically.

There are still a few cases where this general procedure breaks down; we will discuss them in the following paragraphs.

The extreme Case $a = M$ In this case we find

$$\xi = \frac{1}{M}(2Mr - r^2 + M^2), \qquad \eta = \frac{r^3}{M^2}(4M - r). \tag{29}$$

We find $r_{\mathrm{ph}-} = 4M$. The other equatorial photon orbit requires more work. Taking the limit $a/M \to 1$ in equation (26), we would expect the prograde orbit to lie on the horizon at $r = r_+ = M$. As shown in [5, section II], this is not exactly the case: When $a = M$, the coordinate value $r = r_+$ corresponds to an *infinite range of proper distance*. Furthermore, multiple *different* photon orbits are possible at $r = r_{\mathrm{ph}+}$. Namely, a continuum of orbits with $\xi = 2M$ and η varying in the range from 0 to $3M^2$. See also [4, sections II & III]. We will not discuss this feature of the extreme Kerr metric further and refer to the cited literature.

The Schwarzschild Case If $a = 0$, the prograde and retrogade equatorial photon orbit coincide at the radius $r_{\mathrm{ph}} = 3M$ and photon orbits cannot exist at any other radii. This standard result is for instance obtained in [34, section 6.3]. Due to spherical symmetry, photon orbits can occur in any plane through the centre, not just at $\theta = \pi/2$. Since only one r-value is allowed, ξ and η in equations (24) and (25) become indeterminate and we need another procedure to find the shadow edge.

Due to symmetry, the shadow must appear spherical, centered around $\alpha = 0$ and $\beta = 0$. It is therefore sufficient to calculate the radius ρ of the shadow. We choose $\theta_O = \pi/2$ without loss of generality and consider the equatorial photon orbits ($\theta = \pi/2$, $r = 3M$, $\eta = 0$). These rays make up the right- and leftmost parts of the shadow edge: $\alpha = \pm\rho$, $\beta = 0$. We can solve $R = 0$ for ξ:

$$\xi = \pm\sqrt{27}M, \tag{30}$$

another standard result, see for instance [34, section 6.3]. With $\alpha = \pm\xi/\sin(\pi/2)$, we find that the Schwarzschild shadow edge has the radius $\rho = \sqrt{27}M$.

Observer at Poles We consider the case $\theta_O = 0$. $\theta_O = \pi$ is analogous. We follow the approach taken in [15].

Since $\sin\theta_O = 0$, (18) and (19) are indeterminate. This makes sense because the symmetry axis is no longer seen by O and the coordinates α and β are ill-defined. Due to the axial symmetry, the shadow must appear spherical and centered around the axis. Finding its radius will thus be sufficient. All light rays arriving at O require $\xi = 0$. Reasoning similarly as we do in appendix A when deriving the expressions of α and β, we get for large r_O

$$\rho = \left|\frac{d\theta}{dt}\right| r_O^2 = \sqrt{\eta(r_{\xi=0}) + a^2} \tag{31}$$

for the shadow radius. Here $d\theta/dt$ is the θ-component of the ray's regular velocity and $r_{\xi=0}$ is the orbit radius for which $\xi = 0$; $r_{\xi=0}$ is one of the roots of equation (24). The zeros of (24) reduce to the three roots of the third-degree polynomial $M(r^2 - a^2) - r\Delta$. There is only one root outside the horizon, namely

$$r_{\xi=0} = M + 2\sqrt{M^2 - \frac{a^2}{3}}\cos\left[\frac{1}{3}\arccos\left(\frac{3\sqrt{3}M(M^2 - a^2)}{(3M^2 - a^2)^{3/2}}\right)\right]. \tag{32}$$

See [15, section 3]. In the Schwarzschild case we recover $r_{\xi=0} = 3M$ and calculating $\eta(r_{\xi=0})$ using equation (22), we find $\rho = \sqrt{27}M$ as required.

2.2 Shadows of Kerr Black Holes

Using the methods described in the previous section, we can compute the shadow outlines of different Kerr black holes. Figure 3 shows the outlines for $M = 1$ and varying values of a and θ_O. Two main features become apparent: firstly, the shadow is increasingly displaced from the symmetry axis with increasing a and secondly, the shadow becomes asymmetric along the α-direction for large a. Both features disappear as $a \to 0$ with fixed θ_O, where the perfectly round Schwarzschild shadow is recovered as expected. They also disappear for $\theta_O \to 0$ but fixed a and we recover the expected spherical polar case (with radius generally different from the Schwarzschild case as remarked above). We will investigate these two features more closely further down.

The extreme case $a = M$ has an interesting additional feature: the left edge of the shadow contains a completely straight part. These are the photon orbits with different η but same ξ and $r = r_{\mathrm{ph}+}$ we mentioned earlier.

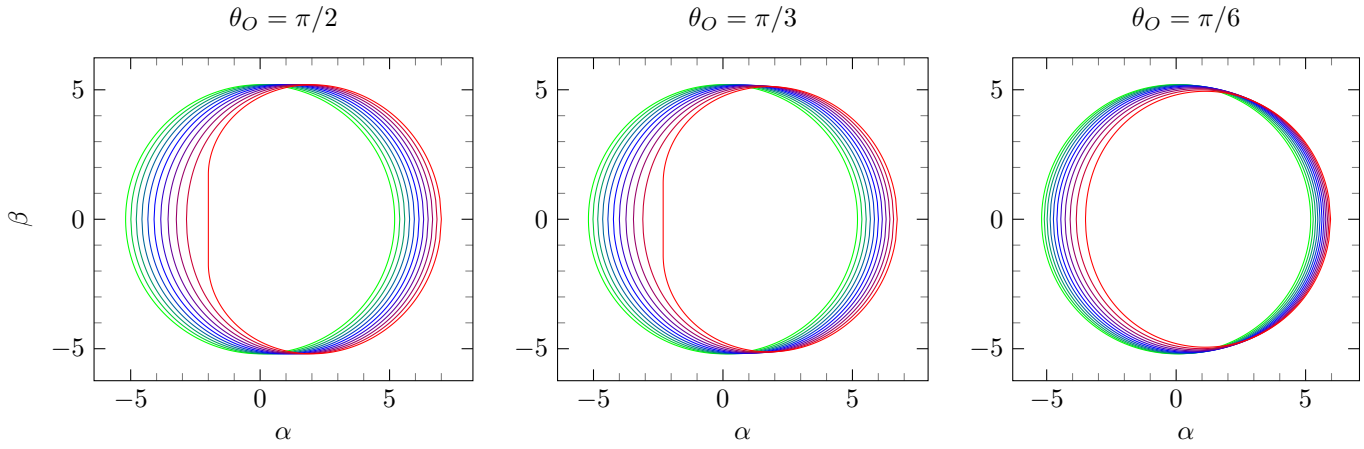

Figure 3: Shadow outlines of a Kerr black hole with $M = 1$ and a varying in the range $[0, 1]$, at fixed values of θ_O. Colours indicate the value of a, in steps of 0.1. Green corresponds to $a = 0$, red to $a = 1$.

Shadows from Numerical Calculations Before we analyze figure 3 further, we note that it is also possible to compute the shadows numerically. For instance, one can solve the geodesic equation of rays incident at O backwards in a process called *ray tracing* to determine their source. An image of the shadow is obtained by colouring all rays originating at the shadow black. Figure 4 shows a basic render of a black hole obtained in this way.

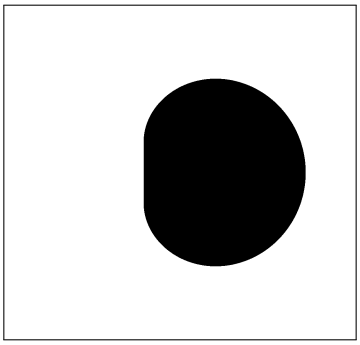

Figure 4: Shadow of a Kerr black hole, $M = a = 1$, seen from $r_O = 100$ and $\theta_O = \pi/2$, with a horizontal and vertical field of view angle of 10°. The image was created using the `cuRRay` GPU-based parallel ray tracing code (available at `https://gitlab.com/sebiG/cuRRay`). The code uses a fourth order Runge-Kutta scheme to numerically solve the geodesic equation and monitors the magnitude of the four-velocity of each geodesic to keep accuracy.

The ray tracing approach is explored in detail for instance in [18] and later [8], as well as in many references therein. Amongst other things, [8] extract shadow outlines from the numerically computed images and arrive at plots identical to figure 3 (in fact, our plot style was inspired by these plots). The first realistically computed image of a (Schwarzschild) black hole was created by Luminet in 1978 [21], also numerically, although not using ray tracing directly.

Horizontal Displacement The displacement of the shadow along the positive α axis can be characterized by the expression [8]

$$D := \frac{\alpha_{\text{min}} + \alpha_{\text{max}}}{2}, \tag{33}$$

where α_{min} and α_{max} are the minimal and maximal α values of the shadow edge. These are the α-intercepts of the shadow curve obtained through (18), (24) and two of the numerically determined zeros of (28). Figure 5 shows D obtained in this semi-analytical way as a function of θ_O, at different fixed values of a. We can see an almost linear dependence of D on both spin parameter a and inclination angle θ_O for small a and θ_O. Figure 5 matches the numerical results in [8], see especially figure 7 therein.

Asymmetry From the plots in figure 3, we observe that the shadow asymmetry is mostly due to the horizontal diameter becoming smaller compared to the vertical diameter, which remains roughly constant. A simple measure of asymmetry is thus the horizontal diameter of the shadow

$$\Delta\alpha := \alpha_{\text{max}} - \alpha_{\text{min}}. \tag{34}$$

α_{max} and α_{min} are again determined semi-analytically. Figure 6 shows $\Delta\alpha$ as a function of θ_O at different values of a. It becomes apparent how most of the shadow distortion happens for high values of a and θ_O close to the equator. The values of the curves at $\theta_O = 0$ correspond to the polar shadow radius from equation (31).

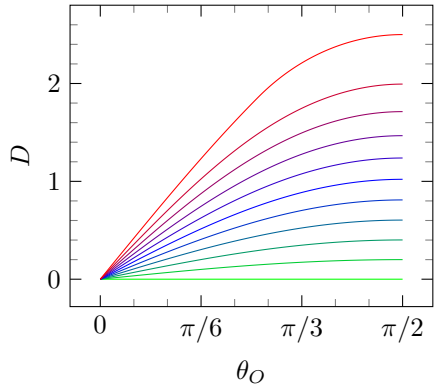

Figure 5: $D(\theta_O)$ for different values of a. Colours distinguish values of a, as in figure 3. $M = 1$.

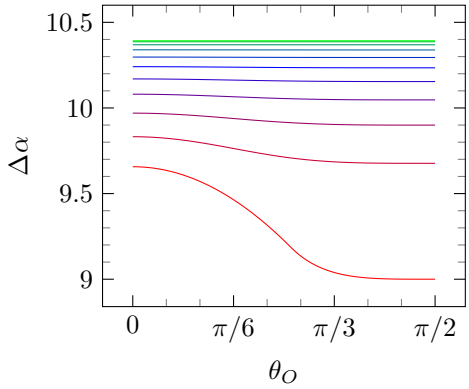

Figure 6: $\Delta\alpha(\theta_O)$ for various values of a; the meaning of the colours is the same as before. $M = 1$.

Scaling with Mass Up to this point, we discussed the case $M = 1$; the more general case of arbitrary M is however not much more difficult. To this end, we consider the effect that varying M has on the shadow, *while keeping the ratio a/M constant*. From (4), (5) and (26) we find that the event horizon radius, static limit radius and the radii of equatorial orbits all scale with M. The range of values of r involved in the equations of section 2.1 thus also scales with M. Continuing in this way, we find that the shadow and thus D and $\Delta\alpha$ all scale with M. We therefore need not discuss general values of M separately. This reflects the available freedom in setting M to one by a suitable choice of units without changing the physics.

Determining Black Hole Properties from Shadows Figure 7 shows contour plots of D and $\Delta\alpha$. We note that the contours intersect; thus if we know D and $\Delta\alpha$ from observations of the shadow, we could determine a and θ_O by finding the intersection of the corresponding contours in the a-θ_O plane of the figure. Unfortunately, D is hard to measure, because the location of the axis of symmetry is generally unknown and cannot be found from visual observations of the shadow alone.

This kind of analysis can however be done with other observables as well, which might

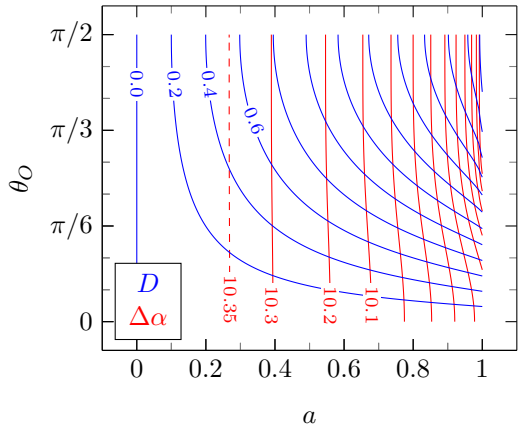

Figure 7: Curves of constant offset D and horizontal diameter $\Delta\alpha$. The values of solid curves of either quantity are evenly spaced (spacing of 0.2 for D and 0.1 for $\Delta\alpha$). $M = 1$.

be easier to measure than D. We will spend most of section 3 discussing different possible observables derived from the shape and size of the shadow that can be used to determine a and θ_O.

2.3 Naked Singularities and Non-Kerr Shadows

Before continuing, we mention here some results concerning shadows of black holes other than Kerr or Schwarzschild. We will not discuss these in detail and refer to the literature.

Naked Singularities If $a > M$ in the Kerr solution, the event horizon disappears and we obtain a naked singularity. Similarly, Kerr-Newman black holes can principally lose their event horizon for certain combinations of the parameters. Shadows of naked singularities in the Kerr metric (and Kerr-Newman metric) have been investigated with similar methods as black hole shadows; see for instance [1], [17] and references therein. Since there is no horizon, it is not directly obvious which parts of the image count as part of the shadow. We can for instance count light rays coming from photon orbits as part of the shadow; this produces an infinitely thin crescent shadow. Without the horizon, the $r < 0$ region in both the Kerr and Kerr-Newman metric becomes visible in principle. Photon orbits mathematically exist in this region and contribute to the shadows: this would lead to a small but extended shadow around the origin of the observer's sky. In a nutshell, we expect vastly different shadows for spinning black holes with horizons and naked spinning singularities. See the references above for further details.

Whether naked singularities can physically exist is debated; the *cosmic censorship hypothesis* [26] for instance claims that they cannot occur.

Exotic Black Holes Besides the well-known metrics of the Kerr-Newman family, a wide range of other black hole solutions have been found. Notably, so-called *regular black holes* are investigated within classical general relativity. For instance by proposing exotic stress tensors, they circumvent the assumptions of the *singularity theorems* [25] and do not exhibit a singularity. See [3] and [2] for examples of a static regular black hole and a rotating regular black hole, respectively. Black holes (static as well as rotating) in other theories than general relativity are also studied; see for instance the references in [29]. It is interesting to note that rotating black hole solutions can sometimes be generated using the so-called *Newman-Janis algorithm* [24][13] starting from an already known static black hole solution. This is how the rotating exotic black holes in the above references were found.

3 Determining Black Hole Properties from Shadows

At the end of section 2.2 we remarked how the horizontal shadow diameter $\Delta\alpha$ and the shadow displacement D can in principle be used to determine the spin parameter a and the observer inclination θ_O. We noted that D is almost impossible to measure in practice but that many different pairs of observables could in principle be used to find these black hole properties. We will discuss some of the observables proposed in the literature and see how black hole properties can be derived from them. We also compare possible advantages and disadvantages of these quantities.

General Setup In what follows, we will assume that at least a part of the shadow outline has been observed (by very large baseline interferometry, say). We will also assume that the distance r_O to the black hole as well as its mass M are known. From an angular length $\tilde{l}$ (for instance the horizontal shadow diameter), we can thus infer the "normalized" length $l = r_O\tilde{l}$ (this is analogous to the normalized coordinates $\alpha = r_O\tilde{\alpha}$ and $\beta = r_O\tilde{\beta}$ we introduced at the beginning). Knowing also the mass, we can scale the observed case to the canonical case $M' = 1$, $a' = a/M$. As noted before, the length l becomes $l' = l/M$ under this scaling.

Once we determined the spin parameter a' in the $M' = 1$ case using contours (this also determines θ_O), we find the actual spin parameter by $a = a'M$.

Although we might know the shape and size of the shadow in the α-β plane, we cannot measure the position of the shadow relative to the centre of the spacetime, as there is no visual feature indicating its position. This is the difficulty when trying to measure the offset D directly.

In short, we will assume to know (parts of) the edge of the shadow as in figure 3 together with the scales of the α and β axes but not the origins of the axes.

3.1 Diameters

We recall the *horizontal shadow diameter*:

$$\Delta\alpha := \alpha_{\max} - \alpha_{\min} = \alpha_R - \alpha_L, \tag{35}$$

where we have introduced the notation L and R for the *leftmost* and *rightmost* points of the shadow edge. Analogously we define the *vertical diameter*:

$$\Delta\beta := \beta_{\max} - \beta_{\min} = \beta_T - \beta_B = 2\beta_T, \tag{36}$$

with B and T being the *bottommost* and *topmost* points of the shadow edge. Due to the symmetry of the shadow, $\beta_B = -\beta_T$. Figure 8 shows the relation between $\Delta\beta$, $\Delta\alpha$ and the points R, L, T and B.

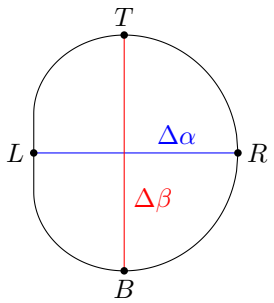

Figure 8: Shadow extremes R, L, T and B as well as shadow diameters $\Delta\alpha$ and $\Delta\beta$.

Computation of $\Delta\beta$ We know the radius ρ of the shadow in the polar case $\sin\theta_O = 0$ from equations (31) and (32). And since the shadow is then circular, $\Delta\beta = 2\rho$. We discuss the case $\sin\theta_O \neq 0$ by largely following the computation in [36, section 3.1].

The positive-β part of the shadow edge can be seen as a curve $\beta(\alpha)$. The topmost point of the shadow then satisfies

$$\frac{\partial\beta}{\partial\alpha} = 0. \tag{37}$$

In section 2.1, α and β were given as a function of a radius parameter r. The above condition can be rewritten as

$$\frac{\partial\beta(r)}{\partial r} \cdot \left(\frac{\partial\alpha(r)}{\partial r}\right)^{-1} = 0. \tag{38}$$

According to equations (18) and (24), $(\partial\alpha/\partial r)^{-1} = 0$ only if $r = M \leq r_{\mathrm{ph}+}$. For $a < M$, $r = M$ is outside the range of relevant photon orbit radii. Only for $a = M$ and $\theta_O = \pi/2$ is $r = M = r_{\mathrm{ph}+}$ a relevant photon orbit radius; we still reject this value as this cannot be the topmost point [8].

[8] $r = M$ contributes to the leftmost part of the shadow edge, not the topmost. Also, $\partial\beta/\partial r$ is undefined there because the shadow edge has a vertical tangent.

From equations (19), (24) and (25) we find after some algebra that $\partial\beta/\partial r = 0$ requires

$$\left[r^3 - 3Mr^2 + 3M^2 r - a^2 M\right] \cdot \left[r^3 - 3Mr^2 + a^2 r\cos^2\theta_O + a^2 M\cos^2\theta_O\right] = 0. \tag{39}$$

The first factor has only one real root, which is smaller than the event horizon radius and thus cannot be the r-value we want. The second factor has one real root:

$$r_{\beta_{\max}} = M + 2\sqrt{M^2 - \frac{a^2}{3}\cos^2\theta_O} \cdot \cos\left[\frac{1}{3}\arccos\left(\frac{3\sqrt{3}M(M^2 - a^2\cos^2\theta_O)}{(3M^2 - a^2\cos^2\theta_O)^{3/2}}\right)\right] \tag{40}$$

(this is equation (3.7) of [36]). It is the required r-value:

$$\Delta\beta = 2\beta(r_{\beta_{\max}}). \tag{41}$$

Particularly for an observer at the equator ($\theta_O = \pi/2$) we get $r_{\beta_{\min}} = 3M$ and $\Delta\beta = 2\sqrt{27}M$, independent of a. Figure 9 shows $\Delta\beta$ for different values of a and θ_O.

We note the similarity between equations (40) and (32): in fact, $r_{\beta_{\max}}$ becomes $r_{\xi=0}$ in the limit $\theta_O \to 0$. This makes intuitive sense: as θ_O approaches 0 (or π), the range of photon orbit radii r relevant for the shadow edge shrinks; until at $\theta_O = 0$, because of symmetry of the shadow, only a single relevant photon orbit radius can remain. This is the one given by $r_{\xi=0}$ in equation (32).

Comment on the Computation of $\Delta\alpha$ In section 2.2 we computed $\Delta\alpha$ numerically from the condition $\beta = 0$. Similarly to the computation of $\Delta\beta$, we could try to solve

$$\frac{\partial\alpha}{\partial\beta} = \frac{\partial\alpha(r)}{\partial r} \cdot \left(\frac{\partial\beta(r)}{\partial r}\right)^{-1} = 0 \tag{42}$$

instead. But because of the square root in (19), this ultimately reduces to solving $\beta = 0$.

$\Delta\alpha$-$\Delta\beta$ Contours In figure 10 we show contours for $\Delta\alpha$ and $\Delta\beta$ in the a-θ_O-plane. Because $\Delta\alpha$ and $\Delta\beta$ only change very little with a for small a (recall figures 6 and 9), their contours are widely spread for small values of a. Contours of $\Delta\beta$ are also sparse for θ_O close

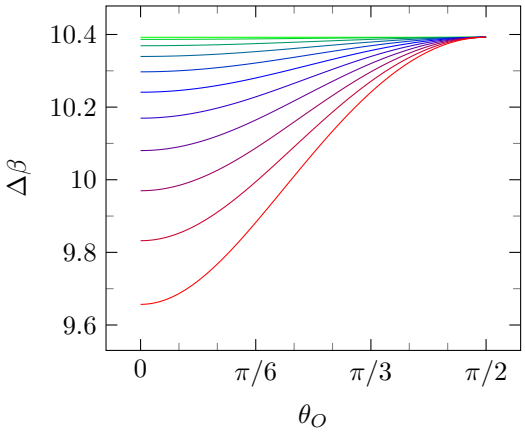

Figure 9: $\Delta\beta(\theta_O)$ for different values of a distinguished by colours, as before. $M = 1$.

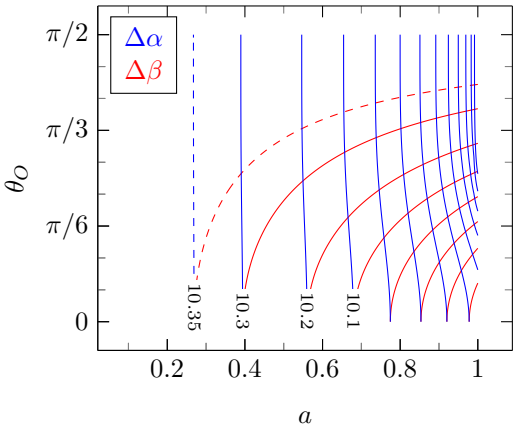

Figure 10: Contours for $\Delta\alpha$ and $\Delta\beta$. Values of solid curves are spaced by 0.1 for both observables. Because of symmetry the sets of curves coincide at $\theta_O = 0$. $M = 1$.

to the horizon, since $\Delta\beta$ becomes independent of a there. We further note that the contours of $\Delta\alpha$ and $\Delta\beta$ coincide for $\theta_O = 0$, stemming from the spherical symmetry of the shadow in the polar case.

To minimize read-off errors, we would like densely packed contours, with the contours of one quantity ideally perpendicular to the other quantity. We thus see that $\Delta\alpha$ and $\Delta\beta$ are most effective for finding a and θ_O, when the actual value of a is high ($\gtrsim 0.5$) and the actual value of θ_O is not too close to the equator or the poles. Since $\Delta\alpha$-contours are approximately vertical, we can use them to determine a even for θ_O close to the equator or the poles; θ_O on the other hand cannot be easily found in these regions.

Another aspect that we will not cover here is the difficulty in measuring $\Delta\alpha$ and $\Delta\beta$ in the first place. Depending on the accuracy with which we can measure these quantities in specific observational situations, the ideal region of parameter space can of course shift and scale.

3.2 Circle Fitting

Next we describe two observables introduced by [17]. Since the shadow appears almost round, they use the points T, R and B to fit a circle; their first observable is its radius ρ_S. As a second observable, they introduce a distortion parameter

$$\delta_S := \Delta_{CS}/\rho_S, \tag{43}$$

where Δ_{CS} is the orthogonal distance from the circle to the point L on the shadow. Figure 11 shows these observables.

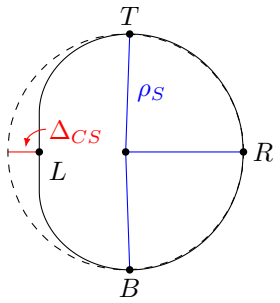

Figure 11: The observables ρ_S and Δ_{CS} introduced by [17], obtained from a circle fitted through the points T, R and B.

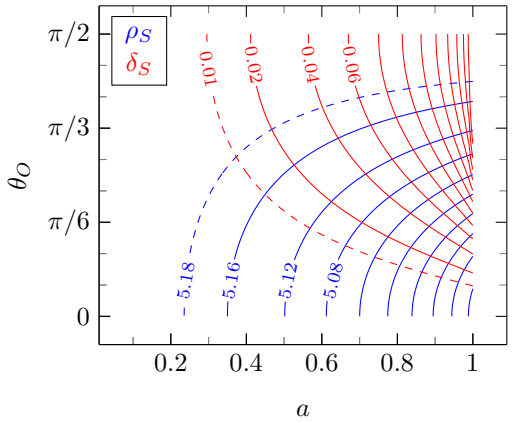

Figure 12: Contours for ρ_S and δ_S. Values of solid curves for ρ_S are spaced by 0.04, for δ_S by 0.02. $M = 1$.

ρ_S-δ_S Contours Both ρ_S and δ_S depend on the coordinates of R and L and thus need to be computed numerically. Figure 12 shows the contours of these two observables. They are the same as computed in [17].

We see that this method is most effective if the real value of a is large and θ_O is not too close to either the equator or the poles. a alone can still be determined close to the equator or the poles due to contours becoming vertical there (if one knows θ_O roughly). In these respects the circle-fitting method is comparable to the $\Delta\alpha$-$\Delta\beta$ method described above.

3.3 Curvature of the Shadow Edge

The previously shown observables require knowledge of the four points L, R, T and B. [36] have shown that as little as two points are required ideally, if the *curvature radius* of the shadow edge at these points is considered as a measurable quantity. This could be an advantage when portions of the shadow edge are obstructed. We show the proposed quantities and their corresponding contours.

Curvature Radius From elementary real analysis we know that the *curvature radius* of a parametric curve $(x(t), y(t))$ in the plane is

$$\rho_C(t) = \left| \frac{(x'^2 + y'^2)^{3/2}}{x'y'' - y'x''} \right|_t . \tag{44}$$

The shadow outline $(\alpha(r), \beta(r))$ is such a curve. Using equations (18), (19), (24) and (25) one finds its curvature radius as a function of r:

$$\rho_C(r) = \frac{64\sqrt{M}(r^3 - a^2 r\cos^2\theta_O)^{3/2}[r(r^2 - 3Mr + 3M^2) - a^2M^2]}{(r-M)^3[3(8r^4 - a^4 - 8a^2r^2) - 4a^2(6r^2 + a^2)\cos(2\theta_O) - a^4\cos(4\theta_O)]}. \tag{45}$$

(this is equation (2.15) in [36]).

Mathematically, the curvature radius at some point on the shadow edge can be obtained from that point and its immediate vicinity alone (any open neighbourhood suffices). In reality, a finite neighbourhood around the point in question is needed due to measurement uncertainty. For instance, one can fit a circle through three points near the point of interest to obtain the curvature radius. So strictly speaking, more than one point on the edge is needed to measure the curvature radius, but they can be relatively close to each other.

Combining Different Curvature Radii We can measure the curvature radius at any point on the shadow edge and use it to determine a and θ_O in principle. Given an image of a shadow, it is however easiest to measure the curvature radii $\rho_{C,L}$, $\rho_{C,R}$, $\rho_{C,T}$ and $\rho_{C,B}$ at the extremal points L, R, T and B respectively, since these points are most readily identified. Figure 13 shows the contours of $\rho_{C,L}$, $\rho_{C,R}$ and $\rho_{C,T}$. We do not need $\rho_{C,B}$ explicitly, since $\rho_{C,B} = \rho_{C,T}$ from symmetry. These contours are precisely those presented by [36].

We note that the curves of $\rho_{C,R}$ resemble those of the fitted shadow radius ρ_S in figure 12, for $\theta_O \lesssim \pi/4$ (which makes sense as the shadow is then almost spherical). While $\rho_{C,R}$ and $\rho_{C,T}$ remain in a finite and quite small range, $\rho_{C,L}$ can get arbitrarily large for $a \to 1$ and $a \to \pi/2$. This reflects the straight left shadow edge occurring in this limit (recall figure 3), which has an infinite curvature radius. Because $\rho_{C,L}$ has the largest range, [36] argue that it might overall be a better observable than $\rho_{C,T}$ or $\rho_{R,T}$.

Combining Diameters and Curvature Radii Another way of determining a and θ_O is through a combination of one diameter and one curvature radius. For this we also need to know at least two points on the shadow edge. Following [36], we choose $\rho_{C,L}$ as curvature radius, since this is the radius with the most variation over the parameter space. As diameter we choose $\Delta\alpha$ because it varies more than $\Delta\beta$ (recall figures 6 and 9). Figure 14 shows the contours of $\rho_{C,L}$ and $\Delta\alpha$. Other combinations of diameters and curvature radii are also possible, see [36].

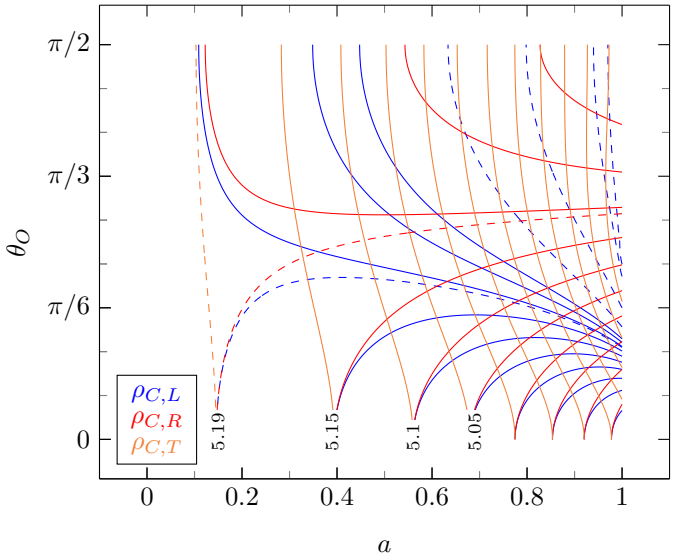

Figure 13: Contours for $\rho_{C,L}$, $\rho_{C,R}$ and $\rho_{C,T}$. Neighbouring solid curves of the same curvature radius are separated by 0.05. At $\theta_O = 0$ the sets of curves all coincide due to symmetry. The dashed blue curves on the top right correspond to $\rho_{C,L} = 5.5$, 6, 8, 10 from left to right. $M = 1$.

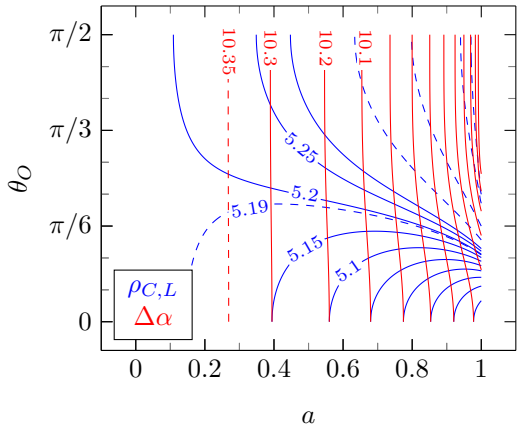

Figure 14: Contours for $\rho_{C,L}$ and $\Delta\alpha$. The spacings are the same as in figures 13 and 10. $M = 1$.

3.4 Observables using the Entire Shadow Edge

Up to this point we considered observables that could be determined from one or two points on the shadow edge. To find a and θ_O, between two and four points are needed. We can also define observables that use *all* points of the edge. While an unobstructed shadow edge is necessary for these observables (although due to symmetry, half of the edge can suffice), they might improve accuracy by using much more of the available data.

We just mention two quantities introduced by [18] and employed by [8] to determine a and θ_O [9]. They define the *average radius*:

$$\langle\rho\rangle := \frac{1}{2\pi}\int_0^{2\pi} \rho(\varphi)\, d\varphi, \tag{46}$$

[9] [18] originally introduced these quantities to propose a test for the *no-hair theorem*.

where $\rho(\varphi) = \sqrt{(\alpha(\varphi) - D)^2 + \beta(\varphi)^2}$, $\tan\varphi = \beta(\varphi)/\alpha(\varphi)$, $(\alpha(\varphi), \beta(\varphi))$ lies on the shadow edge and D is the horizontal displacement of the shadow defined in equation (33). Although D cannot be measured, $\alpha - D$ is measurable. From there the *asymmetry* is defined as

$$A := 2\sqrt{\frac{1}{2\pi}\int_0^{2\pi} (\rho(\varphi) - \langle\rho\rangle)^2 \, d\varphi}. \tag{47}$$

[8] numerically computed images of various Kerr shadows, extracted $\langle\rho\rangle$ and A, fitted empirical models $\langle\rho\rangle(a, \theta_O)$ and $A(a, \theta_O)$, and calculated contours that could be used to read off a and θ_O similarly to the contours discussed above. We will not cover this further, see [8] for more details.

4 Two Applications to M87*

With the release of the VLBI image of the supermassive black hole M87* by the EHT collaboration in early 2019 [9], the theory of shadows we outlined so far has gained in relevance. In fact, the shadow of M87* is clearly visible in the image. We selected two applications of the theory of black hole shadows to the EHT image and summarize them here.

4.1 Ability to Determine a from EHT Image

In [36, section 4] it is estimated whether the shadow in the EHT image can be used to determine the spin parameter of M87* further with the methods described in section 3. Assuming that M87* is a Kerr black hole (which fits well with observations [9, section 8]), [36] begin with the values of M and r_O obtained by the EHT collaboration [11]:

$$M = (6.5 \pm 0.7) \cdot 10^9 \; M_\odot, \qquad r_O = 16.8 \pm 0.8 \text{ Mpc}. \tag{48}$$

The EHT analysis of the accretion disk suggest that the specific spin parameter a/M lies in the range from 0.5 to 0.94 [10]. Furthermore, observations of the energetic jet show an inclination angle of $\theta_O \approx 16°$ [35]. It is interesting to investigate whether a can be further determined using shadow edge techniques.

[36] proceed to describe the values of the observables $\Delta\alpha$, $\Delta\beta$, $\rho_{C,L}$, $\rho_{C,R}$ and $\rho_{C,T}$ for various values of θ_O around 16° and in the possible range of a/M. As we expect from the contours in the last section, variations of the quantities in both a and θ_O are small for $a/M \approx 0.5$ but become more significant for higher a/M. In table 1 we reproduce table 2 of [36], a comparison of the observables for $\theta_O = 16°$ and varying values of a/M. The values in the table can be computed from the formulas of the previous sections; here, the normalized angles have already been converted to real angles in our sky. For a/M between 0.5 and 0.7, changes in the observables are smaller than 1μas; for a/M between 0.7 and 0.94, they are around 1μas or even larger.

The diffraction limit of the EHT is around 25μas [9], but the useful resolution of the M87* image is higher, around 5μas. Still, the current resolution seems to be too low for reasonable measurements of shadow edge observables. [36] argue that if the image resolution is increased to about 1μas in the future, a/M could be well determined at least if the actual spin parameter of M87* happens to be high.

4.2 Ruling out a Naked Singularity

It is interesting to mention that the image of the M87* shadow was also used to rule out the possibility of M87* being a naked singularity [9, section 8]: naked singularities have much smaller shadow sizes than black holes of the same mass (see [1], [17]), incompatible with the observed shadow. The cosmic censorship hypothesis thus seems to hold for M87*.

Table 1: Observables $\Delta\alpha$, $\Delta\beta$, $\rho_{C,L}$, $\rho_{C,T}$ and $\rho_{C,R}$ of the M87* shadow edge with $\theta_O = 16°$ for different possible a/M. All observables are given in μas. Table reproduced from [36, table 2].

a/M	0.5	0.6	0.7	0.8	0.9	0.94
$\Delta\alpha$	38.91	38.64	38.29	37.85	37.28	37.00
$\Delta\beta$	38.96	38.71	38.40	38.03	37.56	37.34
$\rho_{C,L}$	19.51	19.40	19.28	19.14	19.01	18.97
$\rho_{C,T}$	19.50	19.39	19.25	19.08	18.87	18.78
$\rho_{C,R}$	19.43	19.28	19.09	18.84	18.51	18.35

5 Conclusion and Outlook

We have discussed photon orbits in Kerr spacetime following the approach of Carter [7] and derived Bardeen's equations [4] for the edge of the Kerr black hole shadow. We have discussed the shadow in various special cases ($a = M$, $a = 0$ and $\theta_O = 0$) and in the general case.

We went on to describe several shadow observables proposed by [18], [8], [17] as well as [36] and discussed how these observables can be combined to determine the black hole spin a and the observer inclination θ_O. We have seen that some observables require larger portions of the shadow to be visible: $\langle\rho\rangle$ and A need at least half the shadow edge, the observables ρ_S and δ_S obtained from circle-fitting require three or four points respectively, diameters $\Delta\alpha$ and $\Delta\beta$ need two, curvature radii $\rho_{C,L}$, $\rho_{C,T}$ and $\rho_{C,R}$ only one. We also saw that these observables vary in different ways over the parameter space, some more than others. But we also need to keep in mind that in a real-world observation not all observables will be measurable with the same precision and ease. Because of this, none of the observables is clearly superior to the others. Observables will have to be chosen depending on the observational situation at hand.

Although the resolution of the M87* EHT image [9] most likely does not allow us to determine a and θ_O further, we mentioned a rough estimate [36] stating that with a five-fold increase in resolution, this might be possible in the future. If baselines and thus resolutions are increased in the future (for instance with space-based telescopes), shadow observables could be measured more accurately and might become a viable tool in determining parameters of black holes. We also saw that the qualitative shape of the M87* shadow has already been useful in establishing that M87* is not a naked singularity [9].

All in all, we gave an introduction to the theory of Kerr black hole shadows and showcased two recent applications. In closing we mention two aspects that we did not cover. Firstly, we only mentioned shadows of Kerr-Newman black holes, naked singularities and other more exotic and hypothetical objects in passing; see the references given in section 2.3 for details. Secondly, we did not discuss the possibility of using shadows to test general relativity directly; see for instance [27, section 5] for proposed tests using future EHT observations and [16] for an argument showing that some tests cannot be done with today's data.

A Details on Kerr Shadows

We present here some details omitted in the main text. We assume $a \leq M$ throughout.

Celestial Coordinates α and β With some geometry we find

$$\tan\tilde{\alpha} = -\frac{d\phi/dt}{dr/dt} r_O \sin\theta_O, \qquad \tan\tilde{\beta} = \frac{d\theta/dt}{dr/dt} r_O. \tag{49}$$

For large values of r_O spacetime is approximately flat and we have $ds/dt = 1$ (constant speed of light in natural units). Thus,

$$\frac{dr}{dt} = \sqrt{1 - r_O^2 \sin^2\theta_O \left(\frac{d\phi}{dt}\right)^2 - r_O^2 \left(\frac{d\theta}{dt}\right)^2}. \tag{50}$$

For large r_O the shadow is very small and all the relevant light is practically moving radially. The transverse velocity components of a ray are then small compared to the speed of light: $r_O \sin\theta_O \; d\phi/dt \ll 1$ and $r_O \; d\theta/dt \ll 1$. We expand the expression (49) for $\tan\tilde{\alpha}$ in powers of the transverse components:

$$\tan\tilde{\alpha} = -\frac{d\phi}{dt} r_O \sin\theta_O \left(1 + \frac{r_O^2}{2}\left[\left(\frac{d\phi}{dt}\right)^2 \sin^2\theta_O + \left(\frac{d\theta}{dt}\right)^2\right] + \text{higher order terms}\right). \tag{51}$$

The first non-trivial terms are second order, which we can ignore. With $\tan\tilde{\alpha} \approx \tilde{\alpha}$ (shadow is small) and $\alpha := r_O\tilde{\alpha}$ we get

$$\alpha = -\frac{d\phi}{dt} r_O^2 \sin\theta_O = -\frac{u^\phi}{u^t} r_O^2 \sin\theta_O. \tag{52}$$

Similarly,

$$\beta = \frac{u^\theta}{u^t} r_O^2. \tag{53}$$

Equations (6) and (7) essentially state $-E = g_{tt}u^t + g_{t\phi}u^\phi$ and $L = g_{\phi\phi}u^\phi + g_{\phi t}u^t$. We find

$$\frac{u^t}{E} = -\frac{\xi g_{t\phi} + g_{\phi\phi}}{g_{tt}g_{\phi\phi} - g_{t\phi}^2}, \qquad \frac{u^\phi}{E} = \frac{\xi g_{tt} + g_{t\phi}}{g_{tt}g_{\phi\phi} - g_{t\phi}^2}. \tag{54}$$

From equation (14) we also have

$$\frac{u^\theta}{E} = \pm\frac{1}{\Sigma}\sqrt{\eta - \xi^2\cot^2\theta_O + a^2\cos^2\theta_O}. \tag{55}$$

For large r_O,

$$\alpha = -r_O^2 \sin\theta_O \frac{\xi g_{tt} + g_{t\phi}}{-g_{\phi\phi} - \xi g_{t\phi}} \approx -r_O^2 \sin\theta_O \frac{\xi}{r_O^2 \sin^2\theta_O} \tag{56}$$

and

$$\beta = \pm r_O^2 \frac{\sqrt{\cdots}}{\Sigma} \cdot \frac{g_{tt}g_{\phi\phi} - g_{t\phi}^2}{-\xi g_{t\phi} - g_{\phi\phi}} \approx \pm\frac{r_O^2}{r_O^2}\sqrt{\eta - \xi^2\cot^2\theta_O + a^2\cos^2\theta_O}. \tag{57}$$

These are the expressions (18) and (19).

Radial Turning Points of Null Geodesics Null geodesics have at most one radial turning point outside the horizon.

Proof. Since $H = 0$, R is a second degree polynomial with apex at $r = M$. R can have at most one zero with $r > r_+ \geq M$, as there will be another at $2M - r < M$. Since $R = 0$ is required for a radial turning point, there can only be one outside the horizon. □

Conditions for Photon Orbits Assuming that the initial value problem of the geodesic equation has a unique solution, a null geodesic is a photon orbit, if $R = 0$ and $\partial R/\partial r = 0$ hold at a single point along the geodesic.

Proof. A photon orbit is characterized $R = 0$ everywhere. This is equivalent to $R = 0$ at *one point* and $du^r/d\lambda = 0$ everywhere. We can extract the radial component of the geodesic equation by differentiating $\Sigma^2 \cdot (u^r)^2$ by λ:

$$\Sigma^2 2u^r \frac{du^r}{d\lambda} + (u^r)^2\ 2\Sigma \frac{\Sigma}{d\lambda} = \frac{\partial R}{\partial r} u^r, \tag{58}$$

$$\frac{du^r}{d\lambda} = -u^r \frac{1}{\Sigma}\left[\frac{\partial \Sigma}{\partial r} u^r + \frac{\partial \Sigma}{\partial \theta} u^\theta\right] + \frac{1}{2\Sigma^2}\frac{\partial R}{\partial r}, \tag{59}$$

where the last step for now assumes $u^r \neq 0$. This has indeed the shape of a geodesic equation; in particular, the last term depends on u^t and u^ϕ via the constants E and L. It is the most general form of the r-component of the geodesic equation for null goedesics. As such, we could use it to read off the relevant Christoffel symbols.

Instead, we can recover our case of interest, simply by inserting $u^r = 0$. We do not have to worry about proper limits, as the components of $\boldsymbol{u}$ are guaranteed to appear quadratically in the equation. We get

$$\frac{du^r}{d\lambda} = \frac{1}{2\Sigma^2}\frac{\partial R}{\partial r}. \tag{60}$$

(this result is also obtained in [30]) Thus, a geodesic is a photon orbit if and only if $R = 0$ at a single point and $\partial R/\partial r = 0$ everywhere.

Assume now that we have a geodesic with $R = 0$ and $\partial R/\partial r = 0$ at one point; that is, $u^r = 0$ and $du^r/d\lambda = 0$ at this point. Assume also that this geodesic can be computed by solving the initial value problem starting from this point and given the tangent vector (on physical grounds, we would expect this). We see that $r = \text{const.}$ solves equation (60) and hence the radial component of the geodesic equation. But this must be the unique solution, so we have found a photon orbit. □

We could now investigate whether the initial value problem is really well-defined; instead we will note in the next paragraph that it does not matter.

Injection of Light Rays into a Photon Orbits In the main text we argue that certain combinations of ξ and η in the sky of the observer appear black because this combination corresponds to a photon orbit; we use this to find the edge of the black hole shadow. This suggests that we can send a light ray with just the right values of ξ and η towards the black hole to "inject" it into a photon orbit.

If such an injection can happen within a finite amount of affine parameter, the initial value problem would no longer be well-defined for this photon orbit: reversing u^r, u^θ, u^ϕ and a (as we did before, see section 1.3) we would find a valid light ray spontaneously breaking out of the photon orbit. In such a case the conditions $R = 0$ and $\partial R/\partial r = 0$ would no longer be sufficient for photon orbits: while a geodesic with these properties is a photon orbit for some amount of parameter, we cannot tell whether it breaks into another orbit sooner or later.

Such a light ray would still lie on the shadow's edge, it might however not appear black. But whether a light ray on the edge counts towards the shadow or towards the background is completely irrelevant from an observational perspective: the edge is only a one-dimensional curve in the sky.

Equations for η and ξ From equation (15) we find

$$\begin{aligned} 0 = \frac{R}{E^2} &= [(r^2 + a^2) - \xi a]^2 - (r^2 - 2Mr + a^2)[(\xi - a)^2 + \eta] \\ &= r^4 + r^2 a^2 - r^2 \xi^2 - r^2 \eta + 2Mr[(\xi - a)^2 + \eta] - a^2 \eta \end{aligned} \tag{61}$$

and

$$0 = \frac{\partial R}{E^2 \partial r} = 4r^3 + 2r(a^2 - \xi^2 - \eta) + 2M[(\xi - a)^2 + \eta]. \tag{62}$$

Consequently,

$$0 = -\frac{R}{E^2} + r\frac{\partial R}{E^2 \partial r} = 3r^4 + r^2(a^2 - \xi^2 - \eta) + a^2\eta, \tag{63}$$

which gives equation (22). Inserting this into (61), we get the quadratic equation

$$0 = a^2(r - M)\xi^2 - 2Ma(r^2 - a^2)\xi - r^5 + 3Mr^4 - 2r^3a^2 + 2Mr^2a^2 - ra^4 - Ma^4, \tag{64}$$

which has the solutions given in equation (23).

θ-Motion in Null Geodesics All photon orbits in Kerr spacetime fulfil $\eta \geq 0$ and either cross the equator or stay at the equator [10].

Proof. Assume $\eta < 0$. Solving (22) for ξ and using that $r > r_+ \geq M \geq a$, we find $\xi^2 > a^2$. This contradicts the condition $\xi^2 < a^2$ holding if $\eta < 0$. Therefore, $\eta \geq 0$.

Assume $\xi \neq 0$. $\eta \geq 0$ then implies that Θ has two zeros with $\partial\Theta/\partial\theta \neq 0$, opposite from the equator; if $\eta = 0$, there is also a zero with $\partial\Theta/\partial\theta = 0$ at $\theta = \pi/2$ (and possibly two symmetric zeros with $\partial\Theta/\partial\theta$, one on either side of the equator).

Analogously to our analysis of r-motion, a turning point in θ requires $\Theta = 0$ and $\partial\Theta/\partial\theta \neq 0$. Since $\partial\Theta/\partial\theta = 0$ can only possibly coincide with a zero of Θ at the equator, a photon orbit with $\xi \neq 0$ will either (1) be confined to the equator altogether, (2) oscillate between two θ-turning points and repeatedly cross the equator, or (3) periodically reach the axis on one of the hemispheres while confined to this hemisphere. The third option is impossible, since this would require $\xi = 0$.

Assume finally that $\xi = 0$. $\eta \geq 0$ now implies that the only zero of Θ occurs at the equator and $\partial\Theta/\partial\theta = 0$ if $\eta = 0$. Any orbit with $\xi = 0$ must thus eventually reach the equator or be confined to it altogether. □

B Used Software

We used the author's own softwares `cuRRay` and `cuRRay 2` for the creation of figures 4 and 1. They are openly available at `https://gitlab.com/sebiG/cuRRay` and `https://gitlab.com/sebiG/curray2-dev`. `cuRRay` and `cuRRay 2` are not part of this work.

All other plots and contour plots were created using a `python` script specifically created for this work. It is openly available at `https://gitlab.com/sebiG/kerr-shadows`.

[10] See [32] for another approach than the one taken here.

References

[1] Cosimo Bambi and Katherine Freese. Apparent shape of super-spinning black holes. *Physical Review D*, 79:043002, Feb 2009. doi:10.1103/PhysRevD.79.043002.

[2] Cosimo Bambi and Leonardo Modesto. Rotating regular black holes. *Physics Letters B*, 721(4-5):329–334, Apr 2013. doi:10.1016/j.physletb.2013.03.025.

[3] James M. Bardeen. Non-singular general-relativistic gravitational collapse. In *Conference Proceedings of GR5, Tbilisi, USSR*, 1968.

[4] James M. Bardeen. Timelike and null geodesics in the kerr metric. In C. Dewitt and B. S. Dewitt, editors, *Black Holes (Les Astres Occlus)*, pages 215–239. Gordon and Breach, New York, 1973.

[5] James M. Bardeen, William H. Press, and Saul A. Teukolsky. Rotating black holes: Locally nonrotating frames, energy extraction, and scalar synchrotron radiation. *The Astrophysical Journal*, 178:347–369, Dec. 1972. doi:10.1086/151796.

[6] Robert H. Boyer and Richard W. Lindquist. Maximal analytical extension of the Kerr metric. *Journal of Mathematical Physics*, 8(2):265–281, Feb 1967. doi:10.1063/1.1705193.

[7] Brandon Carter. Global structure of the kerr family of gravitational fields. *Physical Review*, 174(5):1559–1571, 1968. doi:10.1103/PhysRev.174.1559.

[8] Chi-Kwan Chan, Dimitrios Psaltis, and Feryal Özel. GRay: A massively parallel gpu-based code for ray tracing in relativistic spacetimes. *The Astrophysical Journal*, 777:13, Nov 2013. doi:10.1088/0004-637X/777/1/13.

[9] Event Horizon Telescope collaboration. First M87 Event Horizon Telescope results. I. The shadow of the supermassive black hole. *The Astrophysical Journal Letters*, 875:L1, Apr 2019. doi:10.3847/2041-8213/ab0ec7.

[10] Event Horizon Telescope collaboration. First M87 Event Horizon Telescope results. V. Physical origin of the asymmetric ring. *The Astrophysical Journal Letters*, 875:L5, Apr 2019. doi:10.3847/2041-8213/ab0f43.

[11] Event Horizon Telescope collaboration. First M87 Event Horizon Telescope results. VI. The shadow and mass of the central black hole. *The Astrophysical Journal Letters*, 875:L6, Apr 2019. doi:10.3847/2041-8213/ab1141.

[12] J. R. Dormand and P. J. Prince. A family of embedded runge-kutta formulae. *Journal of Computational and Applied Mathematics*, 6(1):19–26, 1980. doi:10.1016/0771-050X(80)90013-3.

[13] S. P. Drake and P. Szekeres. Uniqueness of the Newman-Janis algorithm in generating the Kerr-Newman metric. *General Relativity and Gravitation*, 32(3):445–457, 2000. doi:10.1023/A:1001920232180.

[14] Albert Einstein. Die Grundlage der allgemeinen Relativitätstheorie. *Annalen der Physik IV. Folge*, 49(7):769–822, 1916.

[15] Xing-Hui Feng and H. Lü. On the size of rotating black holes. *The European Physical Journal C*, 80:551, Jun 2020. doi:10.1140/epjc/s10052-020-8119-z.

[16] Samuel E. Gralla. Can the EHT M87 results be used to test general relativity? *Physical Review D*, 103:024023, Jan 2021. doi:10.1103/PhysRevD.103.024023.

[17] Kenta Hioki and Kei-ichi Maeda. Measurement of the Kerr spin parameter by observation of a compact object's shadow. *Physical Review D*, 80:024042, Jul 2009. doi:10.1103/PhysRevD.80.024042.

[18] Tim Johannsen and Dimitrios Psaltis. Testing the no-hair theorem with observations in the electromagnetic spectrum. II. Black hole images. *The Astrophysical Journal*, 718:446–454, Jun 2010. doi:10.1088/0004-637X/718/1/446.

[19] Roy P. Kerr. Gravitational field of a spinning mass as an example of algebraically special metrics. *Physical Review Letters*, 11(5):237–238, Sep 1963. doi:10.1103/PhysRevLett.11.237.

[20] L. D. Landau and E. M. Lifschitz. *Lehrbuch der Theoretischen Physik, Band 1: Mechanik*. Verlag Europa Lehrmittel, Haan-Gruiten, 14. edition, 1997. Translated from Russian into German by H. Jungclaussen.

[21] J.-P. Luminet. Image of a spherical black hole with thin accretion disk. *Astronomy and Astrophysics*, 75:228–235, 1979.

[22] Charles W. Misner, Kip S. Thorne, and John Archibald Wheeler. *Gravitation*. W. H. Freeman and Company, San Francisco, 1973.

[23] E. T. Newman, E. Couch, K. Chinnapared, A. Exton, A. Prakash, and R. Torrence. Metric of a rotating, charged mass. *Journal of Mathematical Physics*, 6(6):918–919, 1965. doi:10.1063/1.1704351.

[24] E. T. Newman and A. I. Janis. Note on the Kerr spinning-particle metric. *Journal of Mathematical Physics*, 6(6):915–917, Jun 1965. doi:10.1063/1.1704350.

[25] Roger Penrose. Gravitational collapse and space-time singularities. *Physical Review Letters*, 14(3):57–59, Jan 1965. doi:10.1103/PhysRevLett.14.57.

[26] Roger Penrose. The question of cosmic censorship. In Robert M. Wald, editor, *Black Holes and Relativistic Stars*, chapter 5, pages 103–122. The University of Chicago Press, Chicago and London, 1998.

[27] Dimitrios Psaltis. Testing general relativity with the event horizon telescope. *General Relativity and Gravitation*, 51:137, Oct 2019. doi:10.1007/s10714-019-2611-5.

[28] Karl Schwarzschild. Über das Gravitationsfeld eines Massenpunktes nach der Einsteinschen Theorie. *Sitzungsberichte der Königlich Preussischen Akademie der Wissenschaften zu Berlin*, 7:189–196, 1916.

[29] Rajibul Shaikh. Black hole shadow in a general rotating spacetime obtained through Newman-Janis algorithm. *Physical Review D*, 100:024028, Jul 2019. doi:10.1103/PhysRevD.100.024028.

[30] N. A. Sharp. Comparison of numerical methods for the integration of black hole geodesic equations. *Journal of Computational Physics*, 41:295–308, 1981. doi:10.1016/0021-9991(81)90098-X.

[31] J. L. Synge. The escape of photons from gravitationally intense stars. *Monthly Notices of the Royal Astronomical Society*, 131:463–466, 1966. doi:10.1093/mnras/131.3.463.

[32] Edward Teo. Spherical photon orbits around a Kerr black hole. *General Relativity and Gravitation*, 35(11):1909–1926, Nov 2003. doi:10.1023/A:1026286607562.

[33] Naoki Tsukamoto. Black hole shadow in an asymptotically flat, stationary, and axisymmetric spacetime: The Kerr-Newman and rotating regular black holes. *Physical Review D*, 97:064021, Mar 2018. doi:10.1103/PhysRevD.97.064021.

[34] Robert M. Wald. *General Relativity*. The University of Chicago Press, Chicago and London, 1984.

[35] R. Craig Walker, Philip E. Hardee, Frederick B. Davies, Chun Ly, and William Junor. The structure and dynamics of the subparsec jet in M87 based on 50 VLBA observations over 17 years at 43GHz. *The Astrophysical Journal*, 855:128, Mar 2018. doi:10.3847/1538-4357/aaafcc.

[36] Shao-Wen Wei, Yuan-Chuan Zou, Yu-Xiao Liu, and Robert B. Mann. Curvature radius and Kerr black hole shadow. *Journal of Cosmology and Astroparticle Physics*, 2019(08):030, Aug 2019. doi:10.1088/1475-7516/2019/08/030.